

## Full length article

## Machine learning assisted design of high entropy alloys with desired property

Cheng Wen<sup>a, b, c</sup>, Yan Zhang<sup>a, b</sup>, Changxin Wang<sup>a, b</sup>, Dezhen Xue<sup>d, \*</sup>, Yang Bai<sup>a, b</sup>,  
Stoichko Antonov<sup>a, e</sup>, Lanhong Dai<sup>f</sup>, Turab Lookman<sup>g</sup>, Yanjing Su<sup>a, b, \*\*</sup>

<sup>a</sup> Beijing Advanced Innovation Center for Materials Genome Engineering, University of Science and Technology Beijing, Beijing, 100083, China

<sup>b</sup> Corrosion and Protection Center, University of Science and Technology Beijing, Beijing, 100083, China

<sup>c</sup> School of Mechanical and Power Engineering, Guangdong Ocean University, Zhanjiang, 524000, China

<sup>d</sup> State Key Laboratory for Mechanical Behavior of Materials, Xi'an Jiaotong University, Xi'an, 710049, China

<sup>e</sup> State Key Laboratory of Advanced Metals and Materials, University of Science and Technology Beijing, Beijing, 100083, China

<sup>f</sup> Laboratory for Nonlinear Mechanics of Continuous Media (LNM), Institute of Mechanics, Chinese Academy of Sciences, Beijing, 100080, China

<sup>g</sup> Theoretical Division, Los Alamos National Laboratory, Los Alamos, NM, 87545, USA

## ARTICLE INFO

## Article history:

Received 28 January 2019

Received in revised form

9 March 2019

Accepted 10 March 2019

Available online 12 March 2019

## Keywords:

Multi-principal element alloys

Active learning

Machine learning

Materials genome initiative

## ABSTRACT

We formulate a materials design strategy combining a machine learning (ML) surrogate model with experimental design algorithms to search for high entropy alloys (HEAs) with large hardness in a model Al-Co-Cr-Cu-Fe-Ni system. We fabricated several alloys with hardness 10% higher than the best value in the original training dataset via only seven experiments. We find that a strategy using both the compositions and descriptors based on a knowledge of the properties of HEAs, outperforms that merely based on the compositions alone. This strategy offers a recipe to rapidly optimize multi-component systems, such as bulk metallic glasses and superalloys, towards desired properties.

© 2019 Acta Materialia Inc. Published by Elsevier Ltd. All rights reserved.

## 1. Introduction

The traditional compositional design strategy of alloys always begins with one (or rarely two) principal elements and proceeds by addition of various alloying elements to tailor desired properties [1–3]. Typically, the intrinsic properties of the designed alloy remain dominated by the principal element. For example, Fe acts as the principal element in steels, Ni/Co in superalloys and Ti in titanium alloys [4–6]. High entropy alloys (HEAs) [7,8] are the result of an alloy design approach introduced a decade ago in which multiple elements are mixed in equimolar or near-equimolar compositions to attempt to maximize the configurational entropy. In contrast to the expectation that a large number of intermetallic phases or other complex phases would form in these multi-

principal element alloys, typical HEAs remain a rather simple phase, primarily face centered cubic (FCC), body centered cubic (BCC) or a mixture of the two [9]. This configuration allows for excellent properties of HEAs, including cryogenic toughness, strength and thermal stability at elevated temperatures, as well as good corrosion and wear resistance [10–13].

As HEAs comprise multiple principal elements, the number of possible compositions is much higher than that of conventional alloys [14]. The huge compositional space provides an opportunity to improve properties, such as hardness, but sets a significant challenge in compositional optimization, especially if explored by “trial and error” or intuition [15]. Hence, search strategies that can efficiently and rapidly identify particular alloys with desired properties are necessary. Several efforts have been devoted to utilize thermodynamic modeling, density functional theory (DFT) and molecular dynamics (MD) calculations to guide the alloy design [16–22]. For example, Miracle et al. used the CALPHAD method to predict the formation of phases of HEAs and found that the predicted number of stable phases is twice, or more, than those obtained by experiments [23]. Meanwhile, DFT and MD calculations primarily focus on phase stability, solidification behavior, and

\* Corresponding author.

\*\* Corresponding author. Beijing Advanced Innovation Center for Materials Genome Engineering, University of Science and Technology Beijing, Beijing, 100083, China.

E-mail addresses: [xuedezhen@xjtu.edu.cn](mailto:xuedezhen@xjtu.edu.cn) (D. Xue), [yjsu@ustb.edu.cn](mailto:yjsu@ustb.edu.cn) (Y. Su).

crystallization kinetics of HEAs [24–26]. Moreover, the number of elements, as well as the variety of microstructures, gives rise to complex and computationally intensive calculations compared to conventional alloys. Few of these methods, however, are oriented towards property design, i.e., predicting chemistries and compositions that are optimized for a target property.

Recently, the materials science community has begun to utilize machine learning (ML) tools [27–29], such as identifying structural flow defects in disordered solids and discovering inorganic-organic hybrid materials [30,31]. For HEAs, Tancret et al. [32] proposed a robust strategy to predict the formation of single-phase solid solution HEAs based on a critical assessment of phase formation and a Gaussian process statistical analysis. Their design strategy predicted sixty-two equimolar alloys to form single-phase HEAs. Islam et al., investigated whether a single-phase solid solution, an amorphous phase or an intermetallic compound would form in HEAs by training a neural network model from a dataset of 118 observations with an average predictive accuracy higher than 80% [33]. These studies focus on phase formation predictions, and not on predicting and optimizing the mechanical or functional properties. Besides ML, which estimates the mapping between the property and material features or descriptors, the design of experiments (DOE) using utility functions to select the next experiment is a crucial aspect of sampling the search space in an attempt to find the global optimum, as ML by itself can be sub-optimal [34,35]. This was demonstrated in the search for shape memory alloys (SMAs) with small thermal hysteresis, as well as for BaTiO<sub>3</sub>-based piezoelectrics with large electric field induced strains [36,37].

In the present study, we propose a property-orientated materials design strategy that combines ML and DOE to find alloys with high hardness in the Al-Co-Cr-Cu-Fe-Ni HEA system – a prototype HEA family comprehensively studied thus far [38]. A mixture of various elements results in a broad distribution of hardness ranging from 110 to 770 HV, that is usually unpredictable. In our approach, we first train a ML model to estimate a map between hardness and descriptors, such as chemical compositions and the chemistry of elements. Based on the ML predictions and the associated uncertainties, we employ utility functions to guide the search for alloys with high hardness from a search space of nearly two million possible compositions. Finally, we successfully predict and synthesize several alloys by carrying out an active learning feedback loop with experiments, which we iterate seven times. Our work leads to several alloys with hardness 10% higher than the best value (775 HV) in the original training dataset. In particular, we find that the approach using both the compositions and the descriptors based on a knowledge of the properties of HEAs can effectively accelerate the discovery process compared to using compositions only.

## 2. Design strategy

Our iterative feedback loop for HEAs with optimal design involves a tight coupling with experiments and is schematically shown Fig. 1. The ML, DOE and feedback are combined and implemented as follows: an ML surrogate model is trained based on a dataset containing hardness ( $y$ ) and composition ( $c_i$ ) for each element. The obtained surrogate model (i.e.,  $y_i = f(c_i)$ ) is applied to a search in the materials space, where the hardness is unknown. Based on the hardness predictions and the associated uncertainties, a utility function for selecting the next experiments is employed to choose a candidate for synthesis by balancing exploitation (choosing the material with the highest predicted hardness) and exploration (using the predicted uncertainties to study regions of the search space where the model is less accurate). Subsequent

alloy synthesis and experiments allow an iterative improvement of the surrogate model by incorporating the measured results into the training set. This is represented by Iteration Loop I in Fig. 1. In addition, in order to incorporate more materials descriptors to improve the performance of Iteration Loop I, we describe our alloy not only by the compositions ( $c_i$ ), but also by the use of physical features ( $p_i$ ) of the elements as this is known to be closely related to the hardness. Consequently, the ML surrogate model learns to estimate the property from the compositions as well as these other features, that is,  $y_i = f(c_i, p_i)$ . These features are preselected from a feature pool, which is included in our design strategy as shown by Iteration Loop II in Fig. 1. We compare the performance of these two iteration loops.

## 3. Dataset and experimental method

### 3.1. Data source and quality

We consider HEAs that belong to the Al<sub>x</sub>Co<sub>y</sub>Cr<sub>z</sub>Cu<sub>u</sub>Fe<sub>v</sub>Ni<sub>w</sub> system, where the mole fractions of each element of  $x, y, z, u, v$  and  $w$  is constrained by  $x + y + z + u + v + w = 100\%$ . To minimize the influence of processing on the final property, the training data assembled from the literature are for alloys fabricated by vacuum arc melting only and their property is measured in the as-cast form. In addition, we exclude samples with significant differences in measured hardness. For example, the alloy AlCoCrCu<sub>0.5</sub>FeNi is not considered because its hardness value is reported as 458, 563 and 665 HV in three different studies [39–41]. We use the average value for a composition whose hardness does not vary appreciably in different studies. Examples include the alloy Al<sub>2</sub>CoCrCuFeNi with hardness of 582 and 570 HV [7,42], and AlCoCrFeNi alloy with hardness of 510, 520 and 518 HV [43–45]. Finally, including 18 experimental data from our laboratory, the training data consists in total of 155 samples of measured hardness. The data are fairly scattered and representative, as there are 22 quaternary alloys, 95 quinary alloys and 38 six-component alloys.

After the above preprocessing step, differences in the reported values still remain. This can be attributed to the deviation of the actual composition from the nominal composition, and the variation of the hardness measurement/solidification conditions. As our experimental results are added into the training data in the feedback loop, we take the precaution of synthesizing and characterizing 6 compositions chosen randomly from the training data. The results are listed in Table 1, along with the corresponding literature reported hardness values. The measured hardnesses are consistent with the reported values with a difference of less than 5%. Therefore, the training data from the literature from different laboratories are deemed to be consistent and acceptable for the subsequent steps. The training data is provided in the [supporting information](#).

### 3.2. Search space of allowed, unsynthesized alloys

The possible compositional space of the Al<sub>x</sub>Co<sub>y</sub>Cr<sub>z</sub>Cu<sub>u</sub>Fe<sub>v</sub>Ni<sub>w</sub> system corresponds to a large (virtual) search space, which includes 155 HEAs with measured hardness. The concentrations  $x, y, z, u, v$  and  $w$  are varied with a step size of 1 at.%, given that higher accuracy is not appropriate due to the exploratory nature of the HEA design. The virtual space is constructed by considering the upper and lower compositional limits for alloys with hardness exceeding 500 HV in our training dataset. For example, the concentrations of six-component alloys are constrained within  $15 < x < 47$ ,  $5 < y < 22$ ,  $6 < z < 34$ ,  $5 < u < 16$ ,  $5 < v < 31$  and  $5 < w < 22$  at.%. The unexplored space of yet unsynthesized HEAs thus essentially consists of 1,895,147 alloys with unknown hardness, including 1331

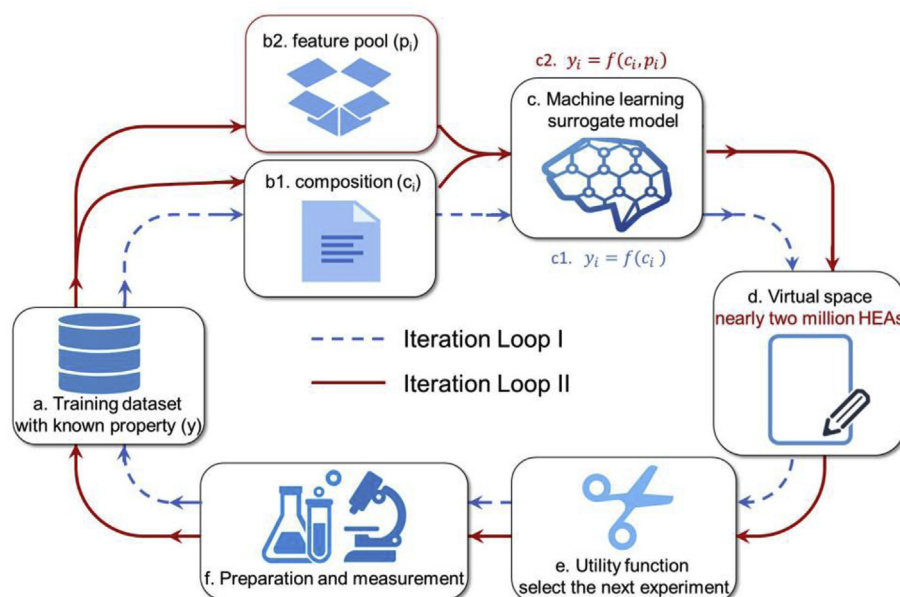


**Fig. 1.** A schematic of the ML and DOE based iterative design loop for accelerated design of HEAs. Iteration Loop I: a ML surrogate model ( $y_i = f(c_i)$ ) is trained with a training dataset and then applied to a search space to predict the property and associated uncertainties. A utility function for DOE is employed to choose a candidate by balancing exploitation and exploration. After the synthesis and measurement of the recommended candidates are performed, the new data are added into the training dataset, allowing the iterative improvement of the surrogate model. Iteration Loop II: the loop is essentially same as Iteration Loop I, except that a feature pool is introduced into Iteration Loop I and a ML surrogate model is trained from the compositions ( $c_i$ ) and the preselected physical features ( $p_i$ ),  $y_i = f(c_i, p_i)$ .

**Table 1**

Comparison of the hardness values between the reported data and experimental data.

Elemental content, at%						Vickers hardness, HV	
Al	Co	Cr	Cu	Fe	Ni	Reported in literature	This work
37.5	12.5	12.5	12.5	12.5	12.5	735 [7]	746 ± 16
20	20	20	10	20	10	604 [40]	594 ± 32
15.8	21.1	21.1	0	21.1	21.1	388 [46]	418 ± 15
22.2	11.1	0	22.2	22.2	22.2	545 [47]	533 ± 31
9.1	0	18.2	18.2	18.2	36.4	238 [48]	259 ± 15
28.6	0	14.3	14.3	14.3	28.6	567 [48]	572 ± 8

quaternary alloys, 218,324 quinary alloys and 1,675,492 six-component alloys. The virtual space with predicted hardness larger than 750 HV can be found in the [supporting information](#).

### 3.3. Experimental procedure

The alloys were prepared by arc-melting the mixtures of high-purity (99.5 wt%) elements in an argon atmosphere. Each ingot was re-melted five times to improve chemical homogeneity. The hardness was measured using a Vickers micro-hardness tester (LECA-VMHT-30M) under a load of 200gf for 15 s holding time. The measurements were repeated ten times for each sample to obtain an average hardness value and statistically significant results. The phase structure was determined by X-ray diffraction (XRD, RigakuSmartLab9000W), while the microstructure of the alloys and the elemental area distributions were analyzed by a scanning electron microscope (SEM, ZEISS EVO18) equipped with an energy dispersive spectrometer (EDS).

## 4. Machine learning and design of experiments

### 4.1. Machine learning models

We employed several well-known machine learning models -

including a linear regression model (lin), a polynomial regression model (poly), support vector regression with a linear kernel (svr.l), a polynomial kernel (svr.p), and a radial basis function kernel (svr.r), a regression tree model (cart), a back propagation neural network model (bpnn) and a k-nearest neighbor model (knn) to produce a non-convex input/output fitness function to estimate the hardness. The best performing model was selected by considering its predictions on an independent testing set (data not used to train the model). We utilized cross validation and the bootstrap method with replacement to estimate the test error for these models.

Our original data was split into a training set and a testing set using different split ratios (training set is taken from 30% to 90% of the original dataset). We calculated the root mean square error

(RMSE) using  $RMSE = \sqrt{\frac{1}{n} \sum_{i=1}^n (y_i - \hat{y}_i)^2}$ , where ( $y_i$ ) is the true value

and ( $\hat{y}_i$ ) the predicted value. This was repeated 100 times for each split of the data. The mean value of RMSE is shown in Fig. 2(a). The error decreases with increasing size of the training set with the three models bpnn, knn and svr.r, outperforming the others across different splitting ratios. The inset of Fig. 2(a) zooms in the performance of three models of svr.r, bpnn and knn.

We also employed the bootstrap with replacement to evaluate the RMSE. The original training data contained  $n = 155$  samples,

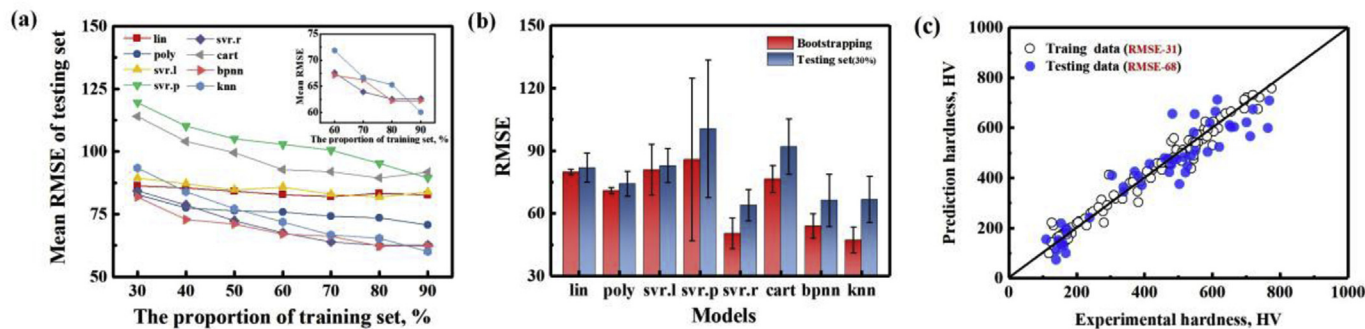


**Fig. 2.** Model evaluation and selection by estimating the test error for different models. (a) a holdout method and (b) bootstrapping methods, indicating svr.r outperforms the others. The inset of (a) zooms in the performance of three models of svr.r, bnn and knn. (c) The predicted values as a function of the measured values of the svr.r model for both training data (randomly chosen 70%) and testing data (the rest 30%).

from which we randomly selected  $n$  observations with replacement to produce a bootstrap sample. We trained a new model on this bootstrap dataset, and made predictions for all the data points in the original training dataset. We repeated this procedure 100 times and obtained 100 sets of predictions for the mean ( $u_i$ ) for the data in the original training set. The RMSE of bootstrap was then estimated from the difference between the mean value, ( $u_i$ ) and the measured value ( $y_i$ ) through  $RMSE = \sqrt{\frac{1}{n} \sum_{i=1}^n (y_i - u_i)^2}$ . Fig. 2(b)

plots the RMSE results from the bootstrap method for all the models using 70% of the training set in Fig. 2(a). The svr.r has the minimum prediction error and its performance is shown in Fig. 2(c). Thus, svr.r was chosen as the model to predict the unexplored alloys in the virtual space in the iterative design loops.

#### 4.2. Utility function for experimental design

As mentioned above, the search space is quite large for the HEA system. It is inadequate to navigate this landscape, searching for a material with an optimal property solely based on the predictions of the ML model. Careful design of experiments is necessary to minimize the number of experiments which need to be carried out in the overall space of variables and parameters (the design space). A utility function can be defined so that an experiment is selected to maximize the expected utility. In the present study, we employed expected improvement (EI) to select the next experiment [35,49]. The EGO algorithm maximizes the expected improvement (EI) over the search space, which is defined by  $EI = E[\max(y - \mu^*, 0)] = \int_{\mu^*}^{\infty} (y - \mu^*) P(y | x') dy = \sigma[\varphi(z) + z\Phi(z)]$ , where  $y - \mu^*$  is the possible improvement for certain  $y$  or hardness,  $P(y | x')$  is the distribution of the predicted  $y$  and is assumed to be normal, and  $z = (\mu - \mu^*)/\sigma$ , where  $\mu^*$  is the maximum value of hardness in the training data,  $\mu$  and  $\sigma$  are the predicted value of hardness and the associated uncertainty, respectively. Because we assume that hardness values are distributed following a normal distribution, EI is expressed in terms of  $\varphi(z)$ , the standard normal density, and  $\Phi(z)$ , the cumulant distribution function. EI balances exploration (aims at improving the predictive model) and exploitation (aims at finding the best prediction). For our preselected model, svr.r, we utilize the bootstrap method from statistics to estimate the uncertainty of predictions,  $\sigma$ . We generate a bootstrap training set by resampling the data from the original training data with replacement. That is, we train 1000 svr.r models based on 1000 bootstrap training datasets to obtain 1000 predictions for each sample in the virtual dataset. The mean predicted value ( $\mu$ ) and standard deviation ( $\sigma$ ) can be estimated from the 1000 predictions to obtain EI (expected improvement) for each alloy.

## 5. Results

### 5.1. Iteration loop I

We performed the iterative feedback loop I seven times using svr.r as the ML model and employing EI for the DOE. We predicted the hardness of all the materials in the virtual space and then selected three of them for the subsequent synthesis and measurement. In total, 21 new alloys were recommended and synthesized, and the compositions are listed in Table S1 of the Supplementary Materials. After each iteration, the measured hardness values of new alloys were added into the training data and the updated svr.r ML model was retrained. The quality of our model predictions is shown in Fig. 3(a), which compares all of the predicted and measured hardness values from the training data and our experimental data. The scatter points distribute around the diagonal line, indicating that the model is adequate and the agreement is reasonable. Fig. 3(b) plots the measured hardness as a function of iteration number. It is noted that even though the three alloys in the first iteration have lower hardness values than the best value of 775 HV in the training data, all of the alloys in the following iterations outperform the training data. In the sixth iteration, the alloy  $Al_{43}Co_{24}Cr_{22}Fe_5Ni_6$  with hardness of 875 HV was discovered. The inset of Fig. 3(b) shows the predicted values for every iteration, which exhibits a similar tendency to the measured results. We conclude that Iterative loop I works well and rapidly leads to a number of HEAs with improved hardness.

### 5.2. Iteration loop II

In Iteration Loop II shown in Fig. 1, we incorporate materials knowledge by introducing descriptors that are also related to mechanical properties of HEAs. This is in contrast to Iteration Loop I that only uses compositions as features. Our objective is to test the efficiency of the search strategy with or without features related to the properties of HEAs.

Several criteria are proposed to describe phase formation in HEAs based on the difference in atomic radii ( $\delta r$ ) between elements, the difference in electronegativity ( $\Delta\chi$ ) between elements, the valence electron concentration (VEC), the mixing enthalpy ( $\Delta H$ ), the configurational entropy ( $\Delta S$ ), the  $\Omega$  parameter (which is related to the entropy, enthalpy and the melting point), the  $\Delta$  parameter (which is related to an atom's configuration on a lattice and its radius) and the  $\gamma$  parameter (the solid angles of atomic packing for the elements with the largest and smallest atomic sizes) [50]. These descriptors are related to the intrinsic properties that influence the formation of a solid solution, amorphous phase and/or



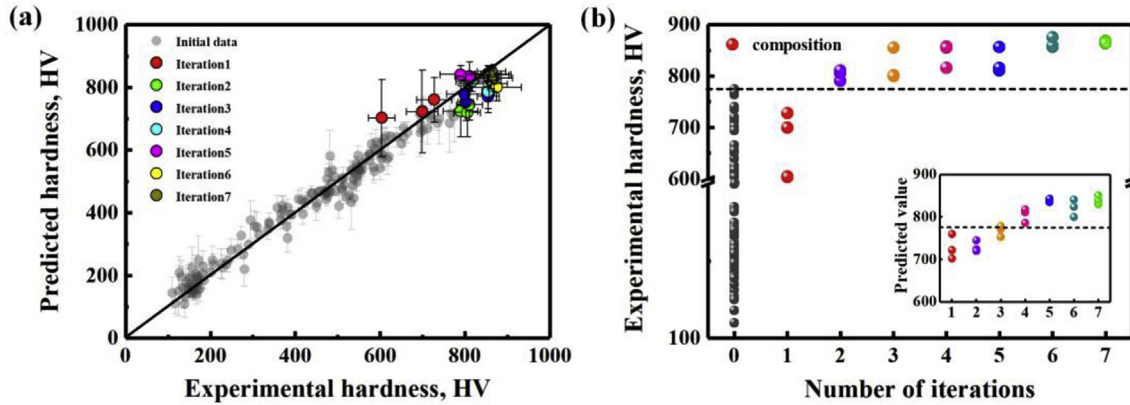


**Fig. 3.** The results of Iterative Loop I. (a) The predicted hardness values versus the measured values for the alloys in the training data and our experimental data. (b) The hardness of the newly synthesized alloys as a function of loop iteration number. The inset of (b) plots the predicted values as a function of iteration number, showing a similar tendency to the measured values.

intermetallic compound in HEAs, and affect the final hardness. We also introduce the local electronegativity mismatch ( $D\chi$ ) between elements, the number of itinerant electrons ( $e/a$ ) and the cohesive energy ( $E_c$ ), all of which potentially relate to phase formation. In addition, we consider parameters from strengthening theory to describe the lattice distortion, elastic misfit and dislocation motion, all of which affect the mechanical properties of HEAs. These features include the modulus mismatch ( $\eta$ ), the local size mismatch ( $D.r$ ), the energy term in the strengthening model ( $A$ ), the Peierls-Nabarro factor ( $F$ ) and sixth square of the work function ( $w$ ) [51–55]. A number of additional descriptors, such as the shear modulus ( $G$ ), the local modulus mismatch ( $D.G$ ), the difference in shear modulus ( $\delta G$ ), and the lattice distortion energy ( $\mu$ ) are also included. Our final feature pool consists of 20 features, 11 of which describe the formation of different phases and the other 9 relate to the mechanical properties. A detailed list of these features is provided in the Supplementary Materials, Table S2.

In order to reduce the computation time and improve model robustness by removing the irrelevant and redundant features, we employ a hybrid method combining a correlation analysis and a wrapper method to perform feature selection. First, for the highly correlated features, we retain only one of them to reduce

redundant information in the subsequent modeling. The right-top corner of Fig. 4(a) depicts the Pearson correlation coefficient map between different features. Those with a correlation coefficient greater than 0.95 were considered as highly correlated. To choose the feature to be retained, we rank the importance of each feature to the model by evaluating the test error of the model with a particular feature. We split our original data into a training set (80%) and a testing set (20%) and build the *svr.r* model based on the training set with one feature. The test error is then calculated

through  $RMSE = \sqrt{\frac{1}{n} \sum_{i=1}^n (y_i - \hat{y}_i)^2}$ , where ( $y_i$ ) is the true value and

( $\hat{y}_i$ ) the predicted value and the test error are ranked in the left-bottom corner of Fig. 4(a). Accordingly, highly correlated features ( $G$ ,  $D\chi$ ,  $\delta G$ ,  $D.G$ ,  $\delta r$ , and  $A$ ) are removed. Second, we further reduce the feature space by considering all possible subsets of these features to identify the subset giving rise to the lowest model error. The cross-validation errors of the *svr.r* model based on different subsets of features are plotted in Fig. 4(b). According to Fig. 4(b), from a starting set of knowledge based features, the initial decrease in error indicates an improvement of the model and the later increase is due to possible over-fitting [56]. The best performance of the model is given by a 6-tuple feature set and what's interesting is

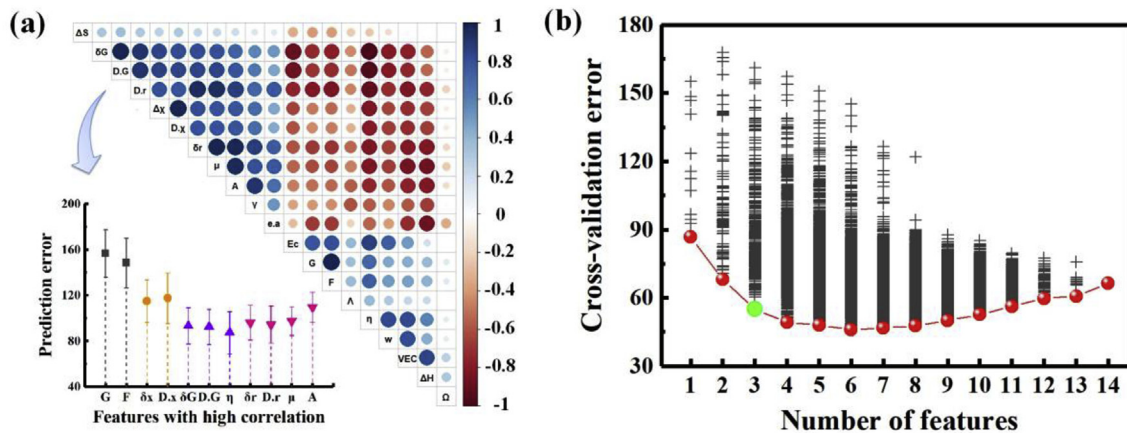


**Fig. 4.** Feature selection to identify the most important features from the feature pool. (a) The Pearson correlation map of the initial twenty features. A larger circle with deeper color indicates a high level of correlation. On the left-bottom panel graph, each color represents features that are highly correlated with each other, and among each color, the one with the lower error is retained. (b) The cross-validation error of each possible *svr.r* model containing a subset of preselected features based on (a). The red frontier tracks the best model for a given number of features. The green dot indicates the set of three features employed in the Iteration loop II, including  $e/a$ ,  $w$  and  $\eta$ . (For interpretation of the references to color in this figure legend, the reader is referred to the Web version of this article.)

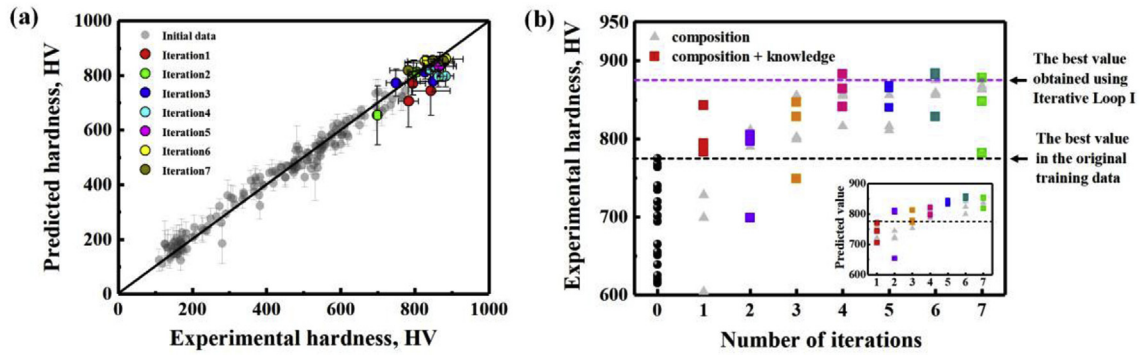


**Fig. 5.** The results of Iterative Loop II. (a) The predicted hardness values versus the measured values for the alloys of the training data and those synthesized in successive iterations. (b) The hardness of the new alloys as a function of iteration number. The black dotted-line represents the best hardness in the training dataset and the magenta dotted-line represents the best value obtained using Iterative Loop I. The inset of (b) plots the predicted values as a function of iteration number, showing a similar tendency to the measured values.

**Table 2**

The top 10 newly predicted and synthesized alloys after seven iterations by both iterative loops. There are more alloys with higher hardness values from Loop II than Loop I.

Alloy No.	Elemental content, at%						Hardness, HV
	Al	Co	Cr	Cu	Fe	Ni	
K6-2	43	22	23	0	7	5	883 ± 47
K4-1	47	20	18	5	5	5	883 ± 22
K6-1	43	22	22	0	8	5	882 ± 22
K7-2	47	19	19	5	5	5	878 ± 25
C6-3	43	24	22	0	5	6	875 ± 58
K5-2 (C7-1)	43	25	22	0	5	5	868 ± 45
K5-1 (C7-2)	43	24	23	0	5	5	865 ± 39
K4-2	43	18	20	0	12	7	864 ± 23
C7-3	43	23	21	0	8	5	863 ± 34
C6-2	47	14	20	5	9	5	859 ± 26

Notes: “C1-2” represents the second alloy in the first iteration of Iteration Loop I, “K1-2” represents the second alloy in the first iteration of Iteration Loop II.

that the best 3-, 4-, 5- and 6-tuple feature sets are ‘e/a, w,  $\eta$ ’; ‘e/a, w,  $\eta$ , vec’; ‘e/a, w,  $\eta$ , vec,  $\Delta S$ ’ and ‘e/a, w,  $\eta$ , vec,  $\Delta S$ ,  $E_c$ ’, respectively. Starting from the best three features, the addition of other features reduces the prediction error of the svr.r model, however, it increases the complexity of the model at the same time, and the improvement of model performance is not obvious. We thus choose the best three features ‘e/a, w,  $\eta$ ’ for simplicity without sacrificing much in terms of the model accuracy and generalizability.

We built our svr.r model with both the composition of each element ( $c_i$ ) and the preselected physical features ( $p_i$ ), i.e.,  $y_i = f(c_i, p_i)$ , utilizing the original training data with  $n = 155$  without including the data of the 21 experimental alloys produced during the Iteration Loop I. This allows us to make a direct comparison between the two Iteration Loops. The original samples are randomly partitioned into 10 equal sized subsamples. Nine subsamples are used as training data and the remaining one subsample is retained as the validation data for testing the model. The cross-validation process is then repeated 10 times to obtain the predicted value ( $\hat{y}_i$ ) of each sample. And the cross-validation error is

estimate through  $RMSE^{CV} = \sqrt{\frac{1}{n} \sum_{i=1}^n (y_i - \hat{y}_i)^2}$ , where ( $y_i$ ) is the

measured value. The svr.r model using both  $c_i$  and  $p_i$  has a cross-validation error of 54.4, which is slightly lower than that 56.3 for the model using only  $c_i$ . Based on this ML surrogate model together with EGO, we perform feedback including synthesis with Iterative loop II seven times as well. Another 21 new alloys are recommended and the compositions are listed in Table S3 of Supplementary Materials.

Fig. 5(a) plots the predicted hardness as a function of the measured values for all the alloys from the training data and those synthesized in successive iterations. The data is closer to the diagonal line compared to Fig. 3(a), indicating that this model is more robust than for Loop I improvement. Fig. 5(b) shows the measured hardness from each iteration from Loop II. In contrast to Iteration

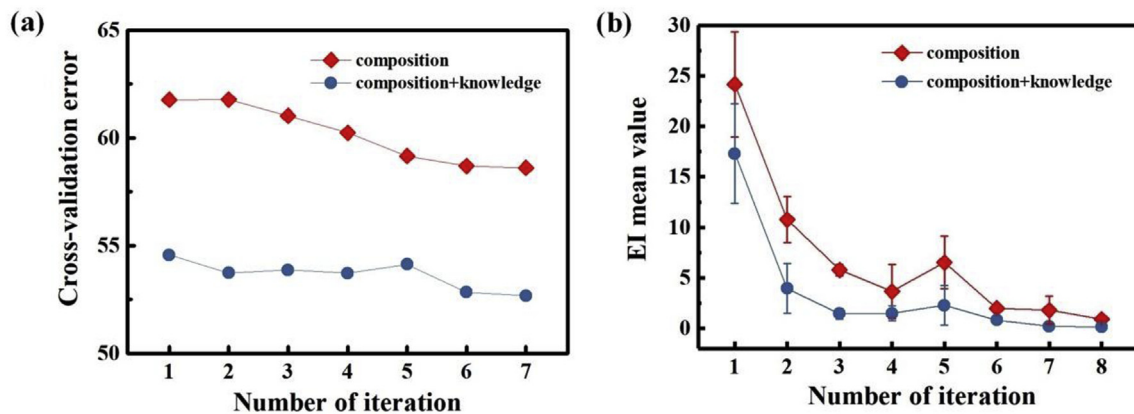


**Fig. 6.** A comparison of the performance of the two iteration loops. (a) The cross-validation error for the svr.r model. The ML model with composition and materials features predicts the target property more accurately. (b) The EI value of the chosen alloys. The mean value and the standard deviation of EI decrease and tend to converge after five iterations for both Iterations Loops.

Loop I, the alloys in the first iteration show better performance than all of the training data and an alloy with hardness of 843 HV is found, which is 8.8% better than the best value in the training data. For each iteration, the hardness obtained in Iteration Loop II is higher than that in Loop I (gray dots in Fig. 5(b)). The alloy,  $\text{Al}_{47}\text{Co}_{20}\text{Cr}_{18}\text{Cu}_5\text{Fe}_5\text{Ni}_5$ , possessing the highest hardness, is predicted after the fourth iteration. Its hardness reaches 883 HV on average, which is 14% higher than the best value in the original dataset and even higher than the best value found by Loop I. The 10 alloys with the highest hardness from the two loops are listed in Table 2. We observe that the alloys (C7-1 and C7-2) obtained in the seventh iteration of Loop I are the same as those (K5-2 and K5-1) obtained in the fifth iteration of Loop II. This indicates that Loop I and II possibly converge to the same optimum in the property-feature space. Overall, Loop II finds HEAs with higher hardness values.

## 6. Discussion

In this study, we address the design of HEAs as an iteration loop combining ML modeling, experimental design algorithms and feedback from experiments. By carrying out the iteration loop, the experimental feedback from each iteration continuously improves the model performance, as shown by the decrease of the cross-validation error for both models in Fig. 6(a).

Meanwhile, the EI (i.e., the expected improvement over the best value observed in the training data) of the newly-made samples gradually decreases with iteration number, indicating that the hardness prediction of our model becomes better, as shown in Fig. 6(b). In addition, the EI values become stable and the alloy compositions tend to stabilize after five iterations for both Iteration Loop I and II. For example, the composition of Al reaches an upper limit, and Cu composition reaches a lower limit of the composition range of our virtual dataset after 5 iterations. This suggests that both search strategies appear to be trending towards a global optimum in the property landscape. Moreover, Iteration Loop II, which utilizes more knowledge based features, performs better than Iteration Loop I using only compositions in terms of the efficiency to find HEAs with higher hardness.

The two alloys,  $\text{Al}_{43}\text{Co}_{22}\text{Cr}_{33}\text{Fe}_7\text{Ni}_5$  and  $\text{Al}_{47}\text{Co}_{20}\text{Cr}_{18}\text{Cu}_5\text{Fe}_5\text{Ni}_5$ , with the highest hardness tend to have more Al content and little Cu. It is known that Cu can promote the formation of FCC phase in HEAs and decrease strength and hardness; Al, when combined with Ni, tends to form a BCC ordered phase due to the high formation enthalpy of these two elements [40]. With an increase of Al content, the HEAs will transform from an FCC solid solution, through a BCC solid solution, to a B2 intermetallic ordered phase, which is expected to possess higher hardness. Our design strategy appears to capture this rule hidden in the training dataset and the design utility function allows us to rapidly identify these alloys.

We checked the phase and the microstructures of the two alloys above. The XRD results in Fig. 7(a) reveal the formation of a mixture of BCC structures, comprised of a disordered BCC solid solution and an ordered BCC (B2 structure), while the SEM micrographs in Fig. 7(b) and the EDS mapping in Fig. 7(c) confirm that the ordered phase can be identified as Al and Ni. This confirms that our design strategy drives the prediction towards the B2 ordered phase. However, in most cases, the ordered B2 structure is not as desirable as the disordered solid solution FCC or BCC phase. Such knowledge can be incorporated into the ML model with a classification filter to prevent searches for alloys likely to be in the intermetallic space.

## 7. Summary

We have proposed a property-orientated materials design

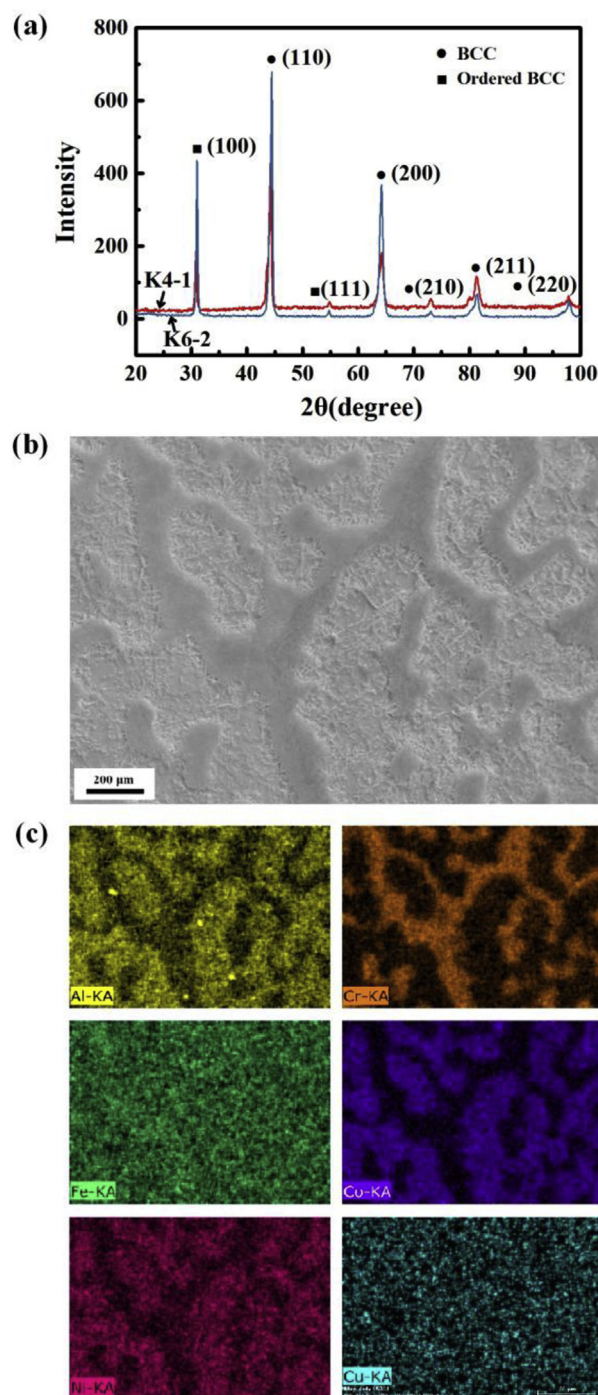


**Fig. 7.** Characterization of the best two alloys  $\text{Al}_{43}\text{Co}_{22}\text{Cr}_{33}\text{Fe}_7\text{Ni}_5$  (K6-2) and  $\text{Al}_{47}\text{Co}_{20}\text{Cr}_{18}\text{Cu}_5\text{Fe}_5\text{Ni}_5$  (K4-1). (a) The XRD spectra shows that both alloys are comprised of a disordered solid solution BCC phase and an ordered B2 phase. (b) Typical SEM micrograph of the K6-2 alloy. (c) An element distribution map of the K6-2 alloy showing that Al, Ni have similar spatial distribution, and Fe distributes uniformly. The combination of Al and Ni tends to form the NiAl ordered B2 phase, leading to the increase of hardness.

strategy combining machine learning, design of experiment and feedback from experiment to search for HEAs with high hardness. The implicit mapping between the target property and descriptors such as chemical compositions and other properties, including those associated with the elements is established through a ML algorithm. Based on the ML predictions and the associated



uncertainties, utility functions are employed to select the new experimental candidates, which are synthesized, measured and augmented the training data. We have demonstrated our iterative, optimization strategy on the HEA system of alloys given by Al-Co-Cr-Cu-Fe-Ni. Out of 42 newly synthesized alloys, we find 35 alloys with hardness values higher than the best value in the training dataset. Amongst these alloys, the hardness of 17 alloys are enhanced by more than 10% compared to the maximum hardness in our training dataset. A comparison of the strategies with different features suggests that learning from composition together with descriptors exploiting knowledge associated with HEAs outperforms that just using composition in terms of accelerating the search for better HEAs. A similar design strategy can be used to optimize other properties, such as light HEAs with high strength and preparation parameters of HEA coatings. The framework can also be extended to bulk metallic glasses and superalloys, which face similar difficulties related to multi-component alloy design.

## Acknowledgements

This work was financially supported by the National Key Research and Development Program of China (Grant No. 2016YFB0700505), National Natural Science Foundation of China (Grant No. 51671157), 111 project (No. B170003) and Los Alamos National Laboratory.

## Appendix A. Supplementary data

Supplementary data to this article can be found online at <https://doi.org/10.1016/j.actamat.2019.03.010>.

## References

- [1] S.C. Huang, Y.S. Zhang, X.L. Zhang, Z.G. Wang, X.Y. Yang, Z. Zeng, Mechanical properties of zirconium-based random alloys: alloying elements and composition dependencies, *Comput. Mater. Sci.* 127 (2017) 60–66.
- [2] A. Inoue, F.L. Kong, S.L. Zhu, C.T. Liu, F. Al, Marzouki, development and applications of highly functional Al-based materials by use of metastable phases, *Mater. Res.* 18 (2015) 1414–1425.
- [3] M.H. Abdelaziz, M. Paradis, A.M. Samuel, H.W. Doty, F.H. Samuel, Effect of aluminum addition on the microstructure, tensile properties, and fractography of cast Mg-based alloys, *Ann. Mater. Sci. Eng.* 2 (2017) 1–10.
- [4] M. Schinhammer, A.C. Hânzi, J.F. Löffler, P.J. Uggowitzer, Design strategy for biodegradable Fe-based alloys for medical applications, *Acta Biomater.* 6 (2010) 1705, 1713.
- [5] H. Long, S. Mao, Y. Liu, Z. Zhang, X. Han, Microstructural and compositional design of Ni-based single crystalline superalloys—A review, *J. Alloy. Comp.* 743 (2018) 203–220.
- [6] A.O.F. Hayama, P.N. Andrade, A. Cremasco, R.J. Contieri, C.R.M. Afonso, R. Caram, Effects of composition and heat treatment on the mechanical behavior of Ti-Cu alloys, *Mater. Des.* 55 (2014) 1006–1013.
- [7] J.W. Yeh, S.K. Chen, S.J. Lin, J.Y. Gan, T.S. Chin, T.T. Shun, C.H. Tsau, S.Y. Chang, Nanostructured high-entropy alloys with multiple principal elements: novel alloy design concepts and outcomes, *Adv. Eng. Mater.* 6 (2004) 299–303.
- [8] B. Cantor, I.T.H. Chang, P. Knight, A.J.B. Vincent, Microstructural development in equiatomic multi-component alloys, *Mater. Sci. Eng., A* 375 (2004) 213–218.
- [9] J.W. Yeh, The Development of High-Entropy Alloys, vol. 27, Hua Kang Journal of Engineering Chinese Culture University, 2011, pp. 1–18.
- [10] B. Gludovatz, A. Hohenwarter, D. Catoor, E.H. Chang, E.P. George, R.O. Ritchie, A fracture-resistant high-entropy alloy for cryogenic applications, *Science* 345 (2014) 1153–1158.
- [11] Y.L. Chou, Y.C. Wang, J.W. Yeh, S.C. Shih, Pitting corrosion of the high-entropy alloy Co<sub>1.5</sub>CrFeNi<sub>1.5</sub>Ti<sub>0.5</sub>Mo<sub>0.1</sub> in chloride-containing sulphate solutions, *Corros. Sci.* 52 (2010) 3481–3491.
- [12] Y.D. Wu, Y.H. Cai, T. Wang, J.J. Si, J. Zhu, Y.D. Wang, X.D. Hui, A refractory Hf<sub>2.5</sub>Nb<sub>2.5</sub>Ti<sub>2.5</sub>Zr<sub>2.5</sub>, high-entropy alloy with excellent structural stability and tensile properties, *Mater. Lett.* 130 (2014) 277–280.
- [13] Y. Yu, J. Wang, J.S. Li, H.C. Kou, H.T. Duan, J. Li, W.M. Liu, Tribological behavior of AlCoCrCuFeNi and AlCoCrFeNiTi<sub>0.5</sub> high entropy alloys under hydrogen peroxide solution against different counterparts, *Tribol. Int.* 92 (2015) 203–210.
- [14] Y.F. Ye, Q. Wang, J. Lu, C.T. Liu, Y. Yang, High-entropy alloy: challenges and prospects, *Mater. Today* 19 (2016) 349–362.
- [15] D.B. Miracle, O.N. Senkov, A critical review of high entropy alloys and related concepts, *Acta Mater.* 122 (2017) 448–511.
- [16] D. Ma, B. Grabowski, F. Körmann, J. Neugebauer, D. Raabe, Ab initio, thermodynamics of the CoCrFeMnNi high entropy alloy: importance of entropy contributions beyond the configurational one, *Acta Mater.* 100 (2015) 90–97.
- [17] C. Zhang, F. Zhang, S. Chen, W. Cao, Computational thermodynamics aided high-entropy alloy design, *JOM (J. Occup. Med.)* 64 (2012) 839–845.
- [18] C. Jiang, B.P. Uberuaga, Efficient ab initio modeling of random multicomponent alloys, *Phys. Rev. Lett.* 116 (2016) 105501.
- [19] J.E. Saal, I.S. Berglund, J.T. Sebastian, P.K. Liaw, G.B. Olson, Equilibrium high entropy alloy phase stability from experiments and thermodynamic modeling, *Scripta Mater.* 146 (2017) 5–8.
- [20] Y. Lederer, C. Toher, K.S. Vecchio, S. Curtarolo, The search for high entropy alloys: a high-throughput ab-initio approach, *Acta Mater.* 159 (2018) 364–383.
- [21] J.M. Sanchez, I. Vicario, J. Albizuri, T. Guraya, J.C. Garcia, Phase prediction, microstructure and high hardness of novel light-weight high entropy alloys, *J. Mater. Res. Technol.* 424 (2018) 1–9.
- [22] A.J.S.F. Tapia, D. Yim, H.S. Kim, B.J. Lee, An approach for screening single phase high-entropy alloys using an inhouse thermodynamic database, *Intermetallics* 101 (2018) 56–63.
- [23] O.N. Senkov, J.D. Miller, D.B. Miracle, C. Woodward, Accelerated exploration of multiprincipal element alloys with solid solution phases, *Nat. Commun.* 6 (2015) 6529.
- [24] A. Sharma, S.A. Deshmukh, P.K. Liaw, G. Balasubramanian, Crystallization kinetics in AlxCrCoFeNi (0 ≤ x ≤ 40) high-entropy alloys, *Scripta Mater.* 141 (2017) 54–57.
- [25] F. Tian, L.K. Varga, L. Vitos, Predicting single phase CrMoW high entropy alloys from empirical relations in combination with first-principles calculations, *Intermetallics* 83 (2017) 9–16.
- [26] X. Sun, H. Zhang, S. Lu, X.D. Ding, Y.Z. Wang, L. Vitos, Phase selection rule for Al-doped CrMnFeCoNi high-entropy alloys from first-principles, *Acta Mater.* 140 (2017) 366–374.
- [27] R. Ramprasad, R. Batra, G. Pilania, A. Mannodikanakthodi, C. Kim, Machine learning in materials informatics: recent applications and prospects, *NPJ Comput. Mater.* 3 (2017) 1–13.
- [28] B. Meredig, A. Agrawal, S. Kirklin, J.E. Saal, J.W. Doak, A. Thompson, K. Zhang, A. Choudhary, C. Wolverton, Combinatorial screening for new materials in unconstrained composition space with machine learning, *Phys. Rev. B* 89 (2014) 1–7.
- [29] Y.T. Sun, H.Y. Bai, M.Z. Li, W.H. Wang, Machine learning approach for the prediction and understanding of glass forming ability, *J. Phys. Chem. Lett.* 8 (2017) 3434–3439.
- [30] E.D. Cubuk, S.S. Schoenholz, J.M. Rieser, B.D. Malone, J. Rottler, D.J. Durian, E. Kaxiras, A.J. Liu, Identifying structural flow defects in disordered solids using machine-learning methods, *Phys. Rev. Lett.* 114 (2015) 108001.
- [31] P. Raccuglia, K.C. Elbert, P.D.F. Adler, C. Falk, M.B. Wenny, A. Mollo, M. Zeller, S.A. Friedler, J. Schrier, A.J. Norquist, Machine-learning-assisted materials discovery using failed experiments, *Nature* 533 (2016) 73–76.
- [32] F. Tancrét, I. Toda-Caraballo, E. Menou, P.E.J.R. Díaz-Del-Castillo, Designing high entropy alloys employing thermodynamics and Gaussian process statistical analysis, *Mater. Des.* 115 (2017) 486–497.
- [33] N. Islam, W.J. Huang, H.L. Zhuang, Machine learning for phase selection in multi-principal element alloys, *Comput. Mater. Sci.* 150 (2018) 230–235.
- [34] T. Lookman, P.V. Balachandran, D.Z. Xue, J. Hogden, J. Theiler, Statistical inference and adaptive design for materials discovery, *Curr. Opin. Solid State Mater. Sci.* 21 (2017) 121–128.
- [35] D.Z. Xue, P.V. Balachandran, J. Hogden, J. Theiler, D.Q. Xue, T. Lookman, Accelerated search for materials with targeted properties by adaptive design, *Nat. Commun.* 7 (2016) 11241.
- [36] D.Z. Xue, D.Q. Xue, R.H. Yuan, Y.M. Zhou, P.V. Balachandran, X.D. Ding, J. Sun, T. Lookman, An informatics approach to transformation temperatures of NiTi-based shape memory alloys, *Acta Mater.* 125 (2017) 532–541.
- [37] R.H. Yuan, Z. Liu, P.V. Balachandran, D.Q. Xue, Y.M. Zhou, X.D. Ding, J. Sun, D.Z. Xue, T. Lookman, Accelerated discovery of large electrostrains in BaTiO<sub>3</sub>-based piezoelectrics using active learning, *Adv. Mater.* 30 (2018) 1702884.
- [38] M.H. Tsai, J.W. Yeh, High-entropy alloys: a critical review, *Mater. Res. Lett.* 2 (2014) 107–123.
- [39] C.C. Tung, J.W. Yeh, T.T. Shun, S.K. Chen, Y.S. Huang, H.C. Chen, On the elemental effect of AlCoCrCuFeNi high-entropy alloy system, *Mater. Lett.* 61 (2007) 1–5.
- [40] G.Y. Ke, Simple Solid Solution in AlxCoCrCu<sub>0.5</sub>FeNiW High-Entropy Alloys, National Tsing Hua University, 2005, pp. 22–98.
- [41] S. Praveen, B.S. Murty, R.S. Kottada, Alloying behavior in multi-component AlCoCrCuFe and NiCoCrCuFe high entropy alloys, *Mater. Sci. Eng., A* 534 (2012) 83–89.
- [42] J.M. Wu, S.J. Lin, J.W. Yeh, S.K. Chen, Y.S. Huang, H.C. Chen, Adhesive wear behavior of AlxCoCrCuFeNi high-entropy alloys as a function of aluminum content, *Wear* 261 (2006) 513–519.
- [43] Z.G. Zhu, K.H. Ma, Q. Wang, C.H. Shek, Compositional dependence of phase formation and mechanical properties in three CoCrFeNi-(Mn/Al/Cu) high entropy alloys, *Intermetallics* 79 (2016) 1–11.
- [44] C. Li, J.C. Li, M. Zhao, Q. Jiang, Effect of aluminum contents on microstructure and properties of AlxCoCrFeNi alloys, *J. Alloy. Comp.* 504S (2010) S515–S518.
- [45] S.G. Ma, Y. Zhang, Effect of Nb addition on the microstructure and properties of AlCoCrFeNi high-entropy alloy, *Mater. Sci. Eng., A* 532 (2012) 480–486.



- [46] Y.F. Kao, T.J. Chen, S.K. Chen, J.W. Yeh, Microstructure and mechanical property of as-cast, -homogenized, and -deformed  $\text{Al}_x\text{CoCrFeNi}$  ( $0 \leq x \leq 2$ ) high-entropy alloys, *J. Alloy. Comp.* 488 (2009) 57–64.
- [47] Y.X. Zhuang, W.J. Liu, P.F. Xing, F. Wang, J.C. He, Effect of Co element on microstructure and mechanical properties of  $\text{FeCo}_x\text{NiCuAl}$  alloys, *Acta. Metall. Sin. (Engl. Lett.)* 25 (2012) 124–130.
- [48] S. Guo, C. Ng, C.T. Liu, Anomalous solidification microstructures in Co-free  $\text{Al}_x\text{CrCuFeNi}_2$  high-entropy alloys, *J. Alloy. Comp.* 557 (2013) 77–81.
- [49] D.R. Jones, M. Schonlau, W.J. Welch, Efficient global optimization of expensive black-box functions, *J. Glob. Optim.* 13 (1998) 455–492.
- [50] S. Guo, Phase selection rules for cast high entropy alloys: an overview, *Mater. Sci. Technol.* 31 (2015) 1223–1230.
- [51] I. Toda-Caraballo, Modelling solid solution hardening in high entropy alloys, *Acta Mater.* 85 (2015) 14–23.
- [52] Z. Wang, Q. Fang, J. Li, Y. Liu, Effect of lattice distortion on solid solution strengthening of BCC high-entropy alloys, *J. Mater. Sci. Technol.* 34 (2018) 349–354.
- [53] C. Varvenne, A. Luque, W.A. Curtin, Theory of strengthening in fcc high entropy alloys, *Acta Mater.* 118 (2016) 164–176.
- [54] G.X. Hu, X. Cai, Y.H. Rong, *Material Science Foundation*, third ed., Shanghai Jiao Tong University Press, Shanghai, 2010, pp. 177–178.
- [55] W.Y. Wang, S.L. Shang, Y. Wang, F.B. Han, K.A. Darling, Y.D. Wu, X. Xie, O.N. Senkov, J.S. Li, X.D. Hui, K.A. Dahmen, P.K. Liaw, L.J. Kecskes, Z.K. Liu, Atomic and electronic basis for the serrations of refractory high-entropy alloys, *NPJ Comput. Mater.* 3 (2017) 2–10.
- [56] S. Geman, E. Bienenstock, R. Doursat, Neural networks and the bias/variance dilemma, *Neural Comput.* 4 (1992) 1–58.